The Transfer Functions of Cardiac Tissue during Stochastic Pacing

Enno de Lange and Jan P. Kucera*
Department of Physiology, University of Bern, Bern, Switzerland

ABSTRACT The restitution properties of cardiac action potential duration (APD) and conduction velocity (CV) are important factors in arrhythmogenesis. They determine alternans, wavebreak, and the patterns of reentrant arrhythmias. We developed a novel approach to characterize restitution using transfer functions. Transfer functions relate an input and an output quantity in terms of gain and phase shift in the complex frequency domain. We derived an analytical expression for the transfer function of interbeat intervals (IBIs) during conduction from one site (input) to another site downstream (output). Transfer functions can be efficiently obtained using a stochastic pacing protocol. Using simulations of conduction and extracellular mapping of strands of neonatal rat ventricular myocytes, we show that transfer functions permit the quantification of APD and CV restitution slopes when it is difficult to measure APD directly. We find that the normally positive CV restitution slope attenuates IBI variations. In contrast, a negative CV restitution slope (induced by decreasing extracellular [K^+]) amplifies IBI variations with a maximum at the frequency of alternans. Hence, it potentiates alternans and renders conduction unstable, even in the absence of APD restitution. Thus, stochastic pacing and transfer function analysis represent a powerful strategy to evaluate restitution and the stability of conduction.

INTRODUCTION

In the heart, action potential (AP) characteristics depend on the rate with which cardiac tissue is excited. Specifically, conduction velocity (CV) and AP duration (APD) depend on one or several previous diastolic or interbeat intervals (IBIs). This rate-dependence, called restitution, is an important determinant of the stability of conduction. In a complex interplay, APD and CV restitution (which can be influenced by antiarrhythmic drugs) determine the occurrence of alternans and functional conduction block, which, in turn, promote wavebreak and reentry. Thus, restitution determines the generation and the stability of reentrant arrhythmias and the transition between tachycardia and fibrillation (1–3).

Forty years ago, Nolasco and Dahlen (4) proposed a model inspired from electrical feedback systems to explain alternans. In this model, APD is related to the previous diastolic interval (DI) by a restitution function f, and alternans occurs when the slope $\alpha = df/dDI$ is ≥ 1 at the point of f for which the sum of APD and DI equals the pacing interval. This theory still inspires numerous studies of alternans and arrhythmogenesis, but it faces the challenge of more recent observations showing that the criterion $\alpha \geq 1$ is not always appropriate to explain and predict alternans.

For example, it was shown that alternans may be absent even if $\alpha > 1$ (5,6). Conversely, it was shown that alternans and wave breakup can occur even if $\alpha < 1$ (7,8). Based on these observations, the concept of restitution was extended with the notion that APD does not solely depend on the previous DI, but, in an intricate manner, on a number of preceding APDs and DIs and on the previous pacing history. Refined restitution models were elaborated by taking into account several preceding APDs and/or DIs and by incorporating memory functions reflecting the progressive adaptation of the AP to a change in pacing rate (9–11). In parallel, increasing evidence supported the notion that intracellular Ca^{2+} cycling is greatly involved in modulating APD and that instabilities of Ca^{2+} cycling can per se constitute a source of alternans (12,13).

These advancements motivated the development of new pacing protocols to explore the relation between APDs and DIs, and their modulation by intracellular Ca^{2+}. One example is the perturbed downsweep protocol (6), which combines pacing at a cycle length decreasing in successive steps with the classical S1-S2 protocol. Further pacing approaches were designed to permit a tight control of the DI, and thus a separation of DI-, APD-, and Ca^{2+}-dependent mechanisms (14–16). Control of the DI was also used to pace cardiac preparations at DIs varying randomly, followed by multiple regression analysis of the successive APDs and DIs, to obtain further information about APD restitution and memory (14,17).

These new approaches, in which cardiac tissue is paced using protocols of increasing complexity, necessitate appropriate models and analyses to untangle the emergent dynamics to fully benefit from these new developments. Besides, the interplay between restitution at the single cell level and the restitution of conduction characteristics, and thus the repercussions on arrhythmogenesis resulting from this interaction, are still not completely understood.

In this article, we establish a mathematical framework to identify, in greater detail, the information that can be obtained by pacing with stimulation intervals that vary stochastically on a beat-to-beat basis. Our framework can be generalized to any restitution paradigm. A further motivation to investigate the possibilities of stochastic pacing is that for

Submitted June 30, 2008, and accepted for publication September 29, 2008.

*Correspondence: kucera@pyl.unibe.ch

Editor: Michael D. Stern.

0006-3495/09/01/0294/18 $2.00

doi: 10.1016/j.bpj.2008.09.025

numerous systems, the best investigative input signal is a signal that varies continuously at all possible frequencies (18). During stochastic pacing, the conjunction of CV restitution characteristics with the restitution of APD modulates activation patterns and thus interbeat intervals. We show that this interaction between CV and APD restitution is revealed in the frequency domain by the transfer function of interbeat intervals between different locations.

Based on this framework, we designed a new approach to characterize restitution and validated it in computer simulations with the Luo-Rudy model (19) and in experiments with patterned strands of cardiac myocytes cultured on microelectrode arrays. Our results show that the transfer function of interbeat intervals provides information about both APD and CV restitution, without the necessity to measure APD, thus opening new possibilities for both experimental and clinical investigations.

We then pursued the aim to investigate the consequences of a decrease of extracellular $[K^+]$ on the stability of interbeat intervals. In both the Luo-Rudy model and the cardiac cell cultures, decreasing $[K^+]_o$ changed the sign of the CV restitution slope from positive to negative, which is characteristic of supernormal conduction (20). In agreement with our theory, this change of sign resulted in amplification of interbeat interval variations with increasing distance from the pacing site, with a maximum for alternans. This result therefore positions supernormal conduction as a mechanism of alternans.

THEORY

In engineering sciences, the transfer function of a linear system characterizes the relation between its input and output in the frequency domain. It describes specifically how the system processes the input to produce the output, provides information about the stability of the system, and permits the derivation of the frequency response of the system in terms of gain and phase shift.

We investigated first how a series of input interbeat intervals t_1, t_2, t_3, … varying around a mean interval t^* (also called basic cycle length, BCL) is processed by cardiac tissue to result in the output of a series of corresponding diastolic intervals d_1, d_2, d_3, … (varying around a mean d^*), action potential durations a_1, a_2, a_3, … (varying around a^*), and local conduction velocities (celerities) c_1, c_2, c_3, … (mean c^*).

By the convention regarding the indices and nomenclature of these variables illustrated in Fig. 1, we have

$$t_n = a_n + d_n. \tag{1}$$

If the tissue is paced at a constant BCL (t^*) and the system is stable, the other variables converge to their respective steady-state values d^*, a^*, and c^*, with $t^* = a^* + d^*$. Restitution characteristics can then be linearized around these steady-state values and thus a linear system is obtained. Assuming that restitution functions of cardiac tissue are only weakly nonlinear around stable steady states, the processing characteristics of this linearized system represent the local processing characteristics of the tissue around these steady-state values.

First-order restitution functions

In its fundamental form, classical (first-order) restitution theory (4) assumes that action potential duration is related to the previous DI by the APD restitution function f. Similarly, CV is related to the previous DI by the CV restitution function g:

$$a_{n+1} = f(d_n) \text{ and } c_{n+1} = g(d_n). \tag{2}$$

We now consider small beat-to-beat variations introduced into the system by varying t_n around its mean value t^*. The variations of t_n, d_n, a_n, and c_n around their steady-state values are defined as $\delta t_n = t_n - t^*$, $\delta d_n = d_n - d^*$, $\delta a_n = a_n - a^*$, and $\delta c_n = c_n - c^*$, respectively. Equation 1 can then be rewritten as

$$\delta t_n = \delta a_n + \delta d_n. \tag{3}$$

By linearizing the expressions in Eq. 2 around their steady-state values, we obtain

$$\delta a_{n+1} = \alpha\, \delta d_n, \tag{4}$$

$$\delta c_{n+1} = \gamma\, \delta d_n, \tag{5}$$

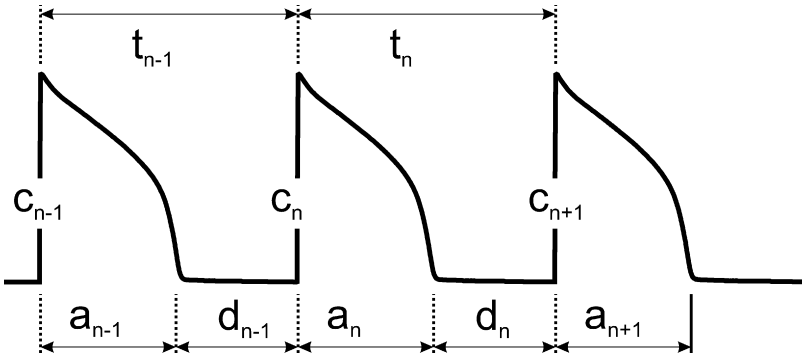

FIGURE 1 Definition, labeling and relationship between interbeat intervals (t), action potential durations (a), diastolic intervals (d), and action potential conduction velocities (c).

in which α and γ are the slopes of the APD and CV restitution functions f and g at $d = d^*$, respectively:

$$\alpha = \frac{\mathrm{d}f(d)}{\mathrm{d}d}\Big|_{d=d^*} \text{ and } \gamma = \frac{\mathrm{d}g(d)}{\mathrm{d}d}\Big|_{d=d^*}. \quad (6)$$

The slopes α and γ are typically established experimentally using a standard S1-S2 protocol, in which the tissue is paced at a constant interbeat interval t^* until steady state is achieved, followed by a modified interval $t \pm \delta t$.

Combining Eqs. 3, 4, and 5, we can write two difference equations describing the evolution of APD and CV given a series of interbeat intervals. Substituting Eq. 3 into Eq. 4, we obtain the difference equation for APD restitution

$$\delta a_{n+1} = \alpha(\delta t_n - \delta a_n), \quad (7)$$

and substituting Eq. 3 into Eq. 5 and using Eq. 7 shifted back one time step, we obtain the difference equation for CV:

$$\begin{aligned} \delta c_{n+1} &= \gamma\delta t_n - \gamma\delta a_n \\ &= \gamma\delta t_n - \gamma\alpha(\delta t_{n-1} - \delta a_{n-1}). \\ &= \gamma\delta t_n - \alpha\delta c_n \end{aligned} \quad (8)$$

Equation 8 thus relates the CV of the next AP with the CV and the interbeat interval of the present one only. This relation lends itself well to be fitted from experimental data using an autoregressive-moving-average (ARMA) model of order 1, with δt_n as input series, δc_n as output series, α as the autoregressive coefficient, and γ as the moving average coefficient. The absence of contributions from APD and DI (δa and δd) in Eq. 8 indicates that identification of the coefficients of the ARMA model based on a known series of interbeat intervals and a corresponding series of measured CV's permits to determine both APD and CV restitution slopes, without the necessity to measure APD and/or DI.

Transfer functions in the case of first-order restitution characteristics

To obtain the transfer functions from t_n to the different observed variables we transform the difference equations to the complex z domain using the Z transform. The advantages of transforming the difference equations to the z domain, rather than treating them directly in the time domain, are that 1), signals in the z domain are characterized by frequency and phase; 2), analysis of the response of discrete-time linear systems in the z domain is more efficient than time-domain methods; and 3), the stability of the system can directly be inferred in the z domain (18).

In the following, $T(z)$, $D(z)$, $A(z)$, and $C(z)$ represent the Z transforms of t_n, d_n, a_n, and c_n, respectively. The Z transforms of Eqs. 7 and 8 are

$$zA(z) = \alpha(T(z) - A(z)), \quad (9)$$

$$zC(z) = \gamma T(z) - \alpha C(z). \quad (10)$$

From the difference relations in the z domain, the transfer functions $H_{t\to a}(z)$ between interbeat intervals and APD, and $H_{t\to c}(z)$ between interbeat intervals and CV are

$$H_{t\to a}(z) = \frac{A(z)}{T(z)} = \frac{\alpha}{z + \alpha}, \quad (11)$$

$$H_{t\to c}(z) = \frac{C(z)}{T(z)} = \frac{\gamma}{z + \alpha}. \quad (12)$$

Also, since $T(z) = A(z) + D(z)$ from Eq. 3, we can compute the transfer function $H_{t\to d}(z)$ from interbeat to diastolic intervals as

$$H_{t\to d}(z) = \frac{D(z)}{T(z)} = \frac{T(z) - A(z)}{T(z)} = 1 - H_{t\to a}(z) \quad (13)$$

and, therefore,

$$H_{t\to d}(z) = \frac{z}{z + \alpha}. \quad (14)$$

All three transfer functions correspond to the same system. They describe the relation between the input quantity (interbeat intervals) and the different observed output variables (APD, CV, and DI; refer to the subscripts) in terms of the complex variable z.

The system is asymptotically stable if the pole $-\alpha$ of the transfer functions lies within the unit circle in the complex plane, i.e., if $|\alpha| < 1$. Conversely, the system is unstable if $|\alpha| > 1$, in accordance with the classical notions of restitution theory. When the pole lies on or very close to the unit circle, the linear system is marginally stable: fluctuations in the input will neither be attenuated, nor amplified. However, in practice, restitution is not absolutely linear and the nonlinearities will determine the stability of the system in this special case.

In the absence of APD restitution (i.e., if APD remains constant), $\alpha = 0$ and the transfer functions simplify to $H_{t\to d}(z) = 1$ (i.e., variations of interbeat intervals translate directly into variations of DI), $H_{t\to a}(z) = 0$ (i.e., APD is constant) and $H_{t\to c}(z) = \gamma/z$.

The derivation of these transfer functions, as presented in this section, can be extended to any higher-order restitution paradigm.

The transfer function of interbeat intervals during AP propagation

In the previous section, we focused on the transfer function $H_{t\to d}(z)$ which relates a series of (controllable) pacing intervals to the corresponding series of DIs at the cellular level. At the multicellular tissue level, DIs will, in turn, directly affect the CV of successive APs. Consequently, beat-to-beat differences in CV will affect the series of interbeat intervals t_n between the passages of the successive APs at a remote location. Because the passages of the wavefront (i.e., activation times) can easily be detected at given locations (e.g., with extracellular or intracellular electrodes), it is of particular interest to investigate the transfer function between interbeat

interval series at two different sites separated by a distance L in a strand sufficiently long and with boundary conditions such that we can ignore the influence of the boundaries.

We assume here that CV is governed by the previous DI, as described in Eqs. 2 and 5. We consider now the variables $t_n(x)$, $d_n(x)$, and $c_n(x)$, representing t_n, d_n, and c_n as a function of distance x, measured along the axis of AP propagation. The conduction time necessary to cover a segment of length $\mathrm{d}x$ amounts to $\mathrm{d}x/c_n(x)$ for the n^{th} wavefront and to $\mathrm{d}x/c_{n+1}(x)$ for the $n+1$st. Thus, over the segment $\mathrm{d}x$, the interbeat interval $t_n(x)$ changes by $\mathrm{d}x/c_{n+1}(x) - \mathrm{d}x/c_n(x)$:

$$\frac{\mathrm{d}t_n(x)}{\mathrm{d}x} = \frac{1}{c_{n+1}(x)} - \frac{1}{c_n(x)}. \tag{15}$$

By introducing the function $j = 1/c$ (i.e., slowness, the reciprocal of CV) with $j^* = 1/c^*$ and $\delta j = j - j^*$, Eq. 15 can be written as

$$\frac{\mathrm{d}t_n(x)}{\mathrm{d}x} = \delta j_{n+1}(x) - \delta j_n(x). \tag{16}$$

Because $\gamma = \mathrm{d}c/\mathrm{d}d = \mathrm{d}g(d)/\mathrm{d}d$ at $d = d^*$ (expressions in Eq. 6), we have

$$\frac{\mathrm{d}j(d)}{\mathrm{d}d}\Big|_{d=d^*} = \frac{\mathrm{d}(1/g(d))}{\mathrm{d}d}\Big|_{d=d^*} = -\frac{\mathrm{d}g(d)/\mathrm{d}d}{(g(d))^2}\Big|_{d=d^*} = -\frac{\gamma}{c^{*2}} \tag{17}$$

and, therefore, the linearization of j around d^* is

$$\delta j_{n+1} = -\frac{\gamma}{c^{*2}}\delta d_n \Leftrightarrow \delta j_n = -\frac{\gamma}{c^{*2}}\delta d_{n-1}. \tag{18}$$

By substitution into Eq. 16, one then obtains

$$\frac{\mathrm{d}t_n(x)}{\mathrm{d}x} = \frac{\gamma}{c^{*2}}(\delta d_{n-1} - \delta d_n). \tag{19}$$

Together with the input $t_n(0)$ and output $t_n(L)$, Eq. 19 is a distributed parameter model; a class of infinite dimensional systems (21). The partial differential equation is of the discrete-time, continuous-space type. By applying the appropriate transformation (either Z transform, or Laplace transform, according to the domain), a transfer function from input to output can be obtained and all notions about poles, zeros, and stability can be applied (18,22).

By applying the Z transformation to Eq. 19 with fixed x, one obtains

$$\begin{aligned}\frac{\mathrm{d}T(z,x)}{\mathrm{d}x} &= \frac{\gamma}{c^{*2}}\left(z^{-1}D(z,x) - D(z,x)\right)\\ &= \frac{\gamma}{c^{*2}}\left(z^{-1}-1\right)D(z,x)\\ &= \frac{\gamma}{c^{*2}}\frac{(1-z)}{z}H_{t\to d}(z)T(z,x).\end{aligned} \tag{20}$$

Assuming that the tissue is homogeneous, integration of Eq. 20 over x gives

$$T(z,x) = T(z,0)\exp\left(\frac{\gamma x}{c^{*2}}\frac{(1-z)}{z}H_{t\to d}(z)\right), \tag{21}$$

and, therefore, the transfer function $H_t(z, L) = T(z, L)/T(z, 0)$ from the stimulation series t_n at $x = 0$ to the output observed at a distance L from the stimulation is

$$H_t(z,L) = \exp\left(\frac{\gamma L}{c^{*2}}\frac{(1-z)}{z}H_{t\to d}(z)\right). \tag{22}$$

Frequency transfer of interbeat interval variations and the stability of conduction

The stability of APD restitution follows from linear stability analysis as shown in the previous sections. When CV restitution is taken into consideration as well, the problem becomes more complicated since one has to analyze the stability of the distributed parameter model defined by Eq. 20. Intuitively, the stability of first-order CV restitution is straightforward: if γ is positive, after pacing at a constant interbeat interval, a premature pulse will conduct slower, therefore widening the interbeat interval toward the steady-state interbeat interval. Conversely, a postmature pulse will catch up its delay by accelerating. However, if γ is negative, the premature pulse will conduct faster than the steady-state ones, therefore speeding up toward its predecessor. In the same way, a postmature pulse will slow down and approach a pulse given at the steady-state interval coming after it. Thus, conduction is unstable for negative γ.

In the discrete time domain, a transfer function $H(z)$ is related to the frequency response function $F(f)$ by $F(f) = H(e^{2\pi if})$, with f in the interval $[0, 1/2]$ (in our situation, $f = 1/2$ corresponds to once every two beats, i.e., the frequency of alternans). Accordingly, the frequency response $F_L(f)$ of interbeat interval variations over a segment of length L is

$$F_L(f) = H_t\left(e^{2\pi if}, L\right) = \exp\left(\frac{\gamma L}{c^{*2}}\left(e^{-2\pi if}-1\right)H_{t\to d}\left(e^{2\pi if}\right)\right). \tag{23}$$

The frequency response can be expressed in terms of gain ($G_L(f)$, in dB) and phase shift ($\Phi_L(f)$, in degrees) as

$$\begin{aligned}G_L(f) &= \frac{20}{\ln 10}\frac{\gamma L}{c^{*2}} \times \Re\left(\left(e^{-2\pi if}-1\right)H_{t\to d}\left(e^{2\pi if}\right)\right),\\ \Phi_L(f) &= \frac{180}{\pi}\frac{\gamma L}{c^{*2}} \times \Im\left(\left(e^{-2\pi if}-1\right)H_{t\to d}\left(e^{2\pi if}\right)\right),\end{aligned} \tag{24}$$

where $\Re$ and $\Im$ denote real and imaginary parts, respectively. Moreover, the frequency response can be normalized by distance L, thereby providing tissue-specific characteristics $G(f)$, the normalized gain (in dB per unit length) and $\Phi(f)$, the normalized phase shift (in degrees per unit length):

$$\begin{aligned} G(f) &= \frac{20}{\ln 10}\frac{\gamma}{c^{*2}} \times \Re\left(\left(e^{-2\pi if}-1\right)H_{t\to d}\left(e^{2\pi if}\right)\right), \\ \Phi(f) &= \frac{180}{\pi}\frac{\gamma}{c^{*2}} \times \Im\left(\left(e^{-2\pi if}-1\right)H_{t\to d}\left(e^{2\pi if}\right)\right). \end{aligned} \tag{25}$$

For the case of first-order restitution (i.e., using $H_{t\to d}(z)$ from Eq. 14), the normalized frequency response is

$$\begin{aligned} G(f) &\quad \frac{20}{\ln 10}\frac{\gamma}{c^{*2}} \times \Re\left(\frac{1-e^{2\pi if}}{\alpha + e^{2\pi if}}\right), \\ \Phi(f) &\quad \frac{180}{\pi}\frac{\gamma}{c^{*2}} \times \Im\left(\frac{1-e^{2\pi if}}{\alpha + e^{2\pi if}}\right). \end{aligned} \tag{26}$$

It appears from Eq. 26 that the stability of conduction is directly related to both the stability of APD restitution ($|\alpha| < 1$) as well as to the sign of γ, which represents the stability of CV restitution. If $\gamma > 0$, the stability follows the second part of the equation, but if $\gamma < 0$, the sign of $G(f)$ is changed and the stability is inverted, rendering a system that is stable at the cellular level unstable. This is in agreement with the intuitive notions formulated at the beginning of this section.

Because of the presence of γ and of the term $e^{-2\pi if} - 1$ in Eqs. 23–26, this condition is distinct from the conditions for stability at the cellular level (poles of $H_{t\to d}(z)$ within the unit circle of the complex plane). This suggests that situations may exist in which cardiac excitation is stable at the cellular level, but conduction itself is intrinsically unstable.

METHODS

Design of a practical implementation

Based on the theory presented above, we implemented the following algorithm to investigate restitution. Cardiac tissue (real or simulated) is paced externally at a given location and the timings of the successive passages of AP wavefronts (activation times) are registered simultaneously at two sites separated by a distance L. These sites are located on a line parallel to AP propagation (orthogonal to the AP wavefronts).

The tissue is first paced at a predefined constant BCL for enough time until a steady-state 1:1 response is established. Subsequently, the tissue is paced at intervals varying stochastically around this BCL according to a Gaussian distribution with a predefined standard deviation (SD). This SD is selected to be large compared to the measurement error on activation times but small enough such that conduction blocks or failure to capture all stimuli does not result. Stochastic pacing is applied for a certain number of cycles (the accuracy of the analysis and the resolution of the frequency response increase with the number of cycles), but for a duration short enough to avoid nonstationarity of the tissue over extended periods of time.

IBI series during stochastic pacing are then calculated at both the proximal and distal recording site and their corresponding (complex) discrete Fourier spectra are computed ($F_{prox}(f)$ and $F_{dist}(f)$). The ratio $F_{dist}(f)/F_{prox}(f)$ corresponds to the frequency response $F_L(f) = H_t(e^{2\pi if}, L)$ in Eq. 23. Gain (in dB) is computed from the decimal logarithm of the magnitude of $F_L(f)$ and phase shift from the argument of $F_L(f)$, respectively. After normalization by L, one therefore obtains the normalized gain $G(f)$ and phase shift $\Phi(f)$ (Eqs. 25 and 26). $G(f)$ and $\Phi(f)$ are then plotted as a function of frequency (Bode plots) for visual interpretation and fitted (according, e.g., to Eq. 26) to identify the restitution slopes.

A flowchart illustrating this approach is presented in the Supplementary Material. The procedure can be repeated using different BCLs and/or for different recording locations.

Computer simulations using coupled maps models

In simulations using coupled maps models, the dynamics of APD were simulated using predefined first-order restitution functions. Conduction was simulated in a one-dimensional cardiac fiber using a predefined CV restitution function g as follows. The fiber was paced at position $x = 0$ using a predefined pacing protocol (see below). This initial condition provided the activation times $t_{a,0}(0)$, $t_{a,1}(0)$,… $t_{a,N}(0)$ at $x = 0$. Using the predefined APD restitution function, repolarization times $t_{r,0}(0)$, $t_{r,1}(0)$,… $t_{r,N}(0)$ and corresponding DIs were computed recursively at $x = 0$. Using the CV restitution function g, propagation of the wavefronts from position x to position $x + dx$ was simulated with a forward Euler approach as $t_{a,i}(x + dx) = t_{a,i}(x) + dx/g(t_{a,i}(x) - t_{r,i-1}(x))$, where i is the number of the wavefront and $t_{a,i}(x) - t_{r,i-1}(x)$ is the corresponding DI at position x. Repolarization times $t_{r,i}(x + dx)$ at position $x + dx$ were again computed using the APD restitution function. By iterating this algorithm, the propagation of wavefronts was computed along the entire length of the cable. Interbeat interval series at a given location in the fiber were computed as the difference series of activation times.

The spatial step dx can be selected to be arbitrarily small and we used a value of 0.01 cm in our simulations. The results were not significantly different when smaller dx were used. Details about the restitution functions used are provided in Results.

Computer simulations using the Luo-Rudy ionic model

Simulations of conduction were conducted in a 1-cm-long fiber of 100 Luo-Rudy phase 1 model cells (19). To obtain CVs and APDs in the range of those observed in cultures of neonatal rat ventricular myocytes, the maximum sodium current conductance (g_{Na}) and the slow inward current conductance (g_{si}) were reduced to 8 and 0.04 mS/cm^2, respectively, as done in previous studies (1,23). The fiber was discretized at the level corresponding to the size of a cell (100 μm) and the lumped myoplasmic and gap junctional intercellular conductance was set to 1.267 μS, as previously published (23,24). Membrane potential (V_m) and other model variables were integrated using a time step of 0.005 ms with the Euler method.

Simulations were run with the normal extracellular potassium concentration of the model ($[K^+]_o$ = 5.4 mmol/L) as well as with decreased $[K^+]_o$ (2.0 mmol/L). The fiber was paced at one extremity (see Pacing Protocols, below). Activation times were defined by depolarization to −35 mV during phase 0 of the AP and APD was measured at repolarization to −80 mV (~95% repolarization for normal $[K^+]_o$, 80% for $[K^+]_o$ = 2.0 mmol/L). APD was determined in the center of the 100-cell strand. CV was determined from the conduction time between cell 25 (x_1 = 0.25 cm) and cell 75 (x_2; $L = x_2 - x_1$ = 0.5 cm). CV was uniform between these two points, as verified by linear regression of activation times versus distance ($r > 0.9999$), indicating that propagation was not influenced by boundary conditions in this segment of the strand.

In vitro experiments

Patterned strands of ventricular myocytes (width: 150 μm) from 1–2 days old Wistar rats were prepared and grown on microelectrode arrays (Sensors, Actuators and Microsystems Laboratory, University of Neuchâtel, Switzerland) as described previously (25,26). The animals were handled in accordance with the ethical principles and guidelines of the Swiss Academy of Medical Sciences. The cardiomyocytes were seeded at a density of 1650 cells/mm^2. The strands were grown on rows of 6 or 12 electrodes (spacing: 1.2 or 0.5 mm, respectively) with a stimulation dipole at their end. As illustrated in Fig. 2, some growth patterns consisted of convolved strands, which were designed to cover the entire set of recording electrodes. This permitted us to map conduction over larger distances.

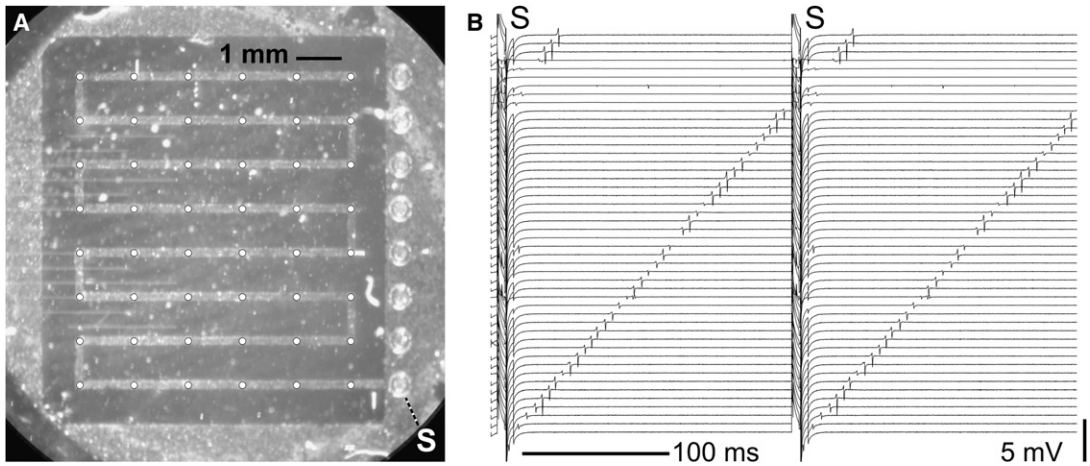

FIGURE 2 Mapping of conduction in patterned cell strands with microelectrode arrays. (*A*) Photograph of a convolved cell strand (length: 5.6 cm). The positions of the recording electrodes are marked with open dots. The preparation was stimulated with the dipole labeled with an *S*. (*B*) AP propagation in the strand after stimulation (*S*). The extracellular electrograms reflect the passage of the AP at each successive electrode. The second wavefront was elicited before the first had reached the end of the strand. Conduction velocity was 25.0 cm/s in this example.

Experiments were performed on 3–5 days old cultures. The strands were first inspected under phase contrast microscopy to verify their structural integrity. Only intact preparations were used. To ensure identical extracellular conditions, the experiments were conducted in Hanks' balanced salts solution. In certain experiments, $[K^+]$ in the Hanks' balanced salts solution (5.8 mmol/L) was reduced to 2.0 or 1.5 mmol/L. The culture chambers, incorporating a connection interface, were then mounted into a custom amplifier array (gain: 1000×) and placed back into the incubator for an equilibration period $\geq$60 min (temperature 36.0 $\pm$ 0.1°C).

The preparations were stimulated with biphasic voltage pulses (26). Extracellular unipolar electrograms were sampled at 10 kHz. Activation times were defined at the occurrence of the minimum of their first derivative (26). Because false detections can exert a tremendous effect on the results, we always took great care to inspect the experimental electrograms visually to ensure that all activations were detected correctly.

Pacing protocols

To establish steady-state conditions in both models and in the experiments, the cell strands were initially paced at a given BCL until all transients had stabilized (1–2 min in the experiments). Subsequently, the strands were subject either to a classical S1-S2 protocol or to a stochastic pacing protocol. In the S1-S2 protocol (used in the Luo-Rudy model strands and the experiments in vitro), isolated deviations δt from BCL were introduced every 10 s, with alternating sign and increasing magnitude. This procedure was repeated for different BCLs. In the stochastic pacing protocol (used in both models and in vitro), cycle length was varied randomly around BCL with a Gaussian distribution characterized by a predefined standard deviation σ. The stochastic protocol was applied for 32–512 cycles in the simulations or during 1–2 min in vitro.

Data Analysis

S1-S2 protocol and restitution slopes

For the Luo-Rudy model strand, APD and CV restitution curves as well as their corresponding slopes α and γ were established using APD/DI in the center of the strand (cell 50) and CV determined from the conduction time between cell 25 and cell 75 ($\Delta x = 0.5$ cm).

In the experiments, CV was determined by linear regression of activation times, as done previously (26). In all the experiments reported here, the number of recording electrodes was $\geq$4 and the correlation coefficient r was >0.99. Because APD could not be measured using the microelectrode arrays, CV restitution curves were represented as CV versus the S1-S2 interval. Since we paced the preparations for 1–2 min at each investigated BCL before applying the S1-S2 protocol and because the modified intervals were introduced only every 10 s (corresponding in all experiments to at least 40 cycles), we assumed that APD had returned to its steady-state value (for each given BCL) before the S1-S2 intervals. Under this assumption, the CV versus S1-S2 curve for a particular BCL is a shifted version of the corresponding CV versus DI curve, with the same shape and slope. The CV restitution slope γ was determined for each BCL tested by fitting the exponential function $CV(\mathrm{S1S2}) = a + b\exp(-\mathrm{S1S2}/c)$ to the CV data points for the different S1-S2 intervals. The slope γ was defined as the slope of this function at S1S2 = BCL.

Stochastic pacing protocol and transfer functions of interbeat interval variations

In the computer simulations, the frequency transfer of interbeat intervals variations ($F_L(f)$, see Eq. 23) was computed as the ratio of the discrete fast Fourier transforms of corresponding series of 128–512 interbeat intervals registered 0.25 and 0.75 cm away from the stimulation site ($L = 0.5$ cm). The restitution slopes α and γ were estimated from times series of IBIs and CVs using ARMA model identification of the first-order difference Eq. 8 with a classical least-squares algorithm. Details concerning this algorithm are provided in Data S1.

In the experiments, the two electrodes that were most distant from each other and that exhibited a signal/noise ratio large enough to reliably identify activation times were selected for this analysis (interelectrode distance: L). $F_L(f)$ was computed as the ratio of Welch power spectra of corresponding series of 64–256 interbeat intervals registered at these two electrodes.

In all analyses, the computed $F_L(f)$ were then normalized by L to provide the tissue-specific normalized transfer spectra characterized by $G(f)$ and $\Phi(f)$ (Eq. 25), which were represented in Bode plots.

Statistics

Unless specified otherwise, data are presented as mean $\pm$ SD. The value n represents the number of distinct preparations used. Significance was assessed at the $p < 0.05$ level by the examination of 95% confidence intervals.

RESULTS

Transfer functions of interbeat interval variations in a linear coupled maps model

To verify our derivation of the transfer function of interbeat interval (IBI) variations between two sites separated by a distance L, we first conducted simulations of conduction in a cell strand using a first-order coupled maps model. APD and CV were defined as linear functions of the previous DI as

$$\begin{aligned} a_{n+1} &= a^* + \alpha(d_n - d^*) \\ c_{n+1} &= c^* + \gamma(d_n - d^*) \end{aligned} \quad (27)$$

with $a^* = 80$ ms, $d^* = 80$ ms, $c^* = 30$ cm/s, and $t^* = 160$ ms. The strand was paced at position $x = 0$ at intervals varying randomly around t^* with a SD of 5 ms, and IBI series were registered at positions $x_1 = 0.25$ cm and $x_2 = 0.75$ cm.

In a first series of simulations, the effects of CV restitution alone were studied by setting α to 0 (no APD restitution) and by varying γ between -0.1 and $+0.1$ cm/s/ms (because in cardiac electrophysiology, CV is usually expressed in cm/s and time in ms, we express γ in cm/s/ms). The corresponding CV restitution relationships are shown in Fig. 3 *A*. Fig. 3 *B* illustrates a series of 50 successive IBIs registered at x_1 and x_2 for a positive value of γ of $+0.1$ cm/s/ms and a negative value of -0.1 cm/s/ms, respectively. For $\gamma = +0.1$ cm/s/ms, peak-to-peak IBI variations were decreased by ~9% between x_1 and x_2. In contrast, for $\gamma = -0.1$ cm/s/ms, IBI variations were increased by ~15%. Moreover, as illustrated in Fig. 3 *C*, IBI variations exhibited a phase lag at position x_2 relative to x_1 for $\gamma = +0.1$ cm/s/ms, and, conversely, IBI variations were characterized by a phase advance at x_2 for $\gamma = -0.1$ cm/s/ms.

The changes in IBI variations were examined in terms of normalized gain and phase shift between x_1 and x_2 using Bode plots, as in Fig. 3 *D*. For positive values of γ, attenuation of IBI variations was reflected by a frequency-dependent negative gain, and accompanied by a frequency-dependent negative phase shift (i.e., a phase lag at x_2 relative to x_1). The attenuation was maximal at a frequency f of 0.5 beat^{-1}, the phase lag was maximal at $f = 0.25$ beat^{-1}, and the frequency response scaled proportionally to γ. Conversely, for negative values of γ, the Bode plots exhibited the same characteristics as for $\gamma > 0$ but for a change of sign. The gain was positive with a maximum at $f = 0.5$ beat^{-1} and the phase was advanced.

The normalized frequency response predicted theoretically ($G(f)$ and $\Phi(f)$ in Eq. 26), shown in Fig. 3 *D* as thick shaded curves, was congruent for all values of γ with the frequency response simulated in the coupled maps model during stochastic pacing.

Influence of first-order APD restitution on the transfer function of interbeat interval variations

In a similar approach, the linear coupled maps model was used to simulate the effects of first-order APD restitution on the transfer function. In the set of simulations presented in Fig. 4, γ was assigned a constant positive or negative value ($+0.03$ and -0.03 cm/s/ms, respectively) and α was varied in the interval $[-1, 1]$. The corresponding transfer functions, computed by spectral analysis from the stochastic pacing simulations, are represented in Fig. 4 *B* together with the frequency response predicted theoretically. Once more, the simulated and predicted responses were congruent.

Interestingly, APD restitution resulted in a distortion of the response curves. Positive values of α, commonly encountered in cardiac electrophysiology, skewed the curves toward the right and magnified the effect of CV restitution on the right-hand side of the spectrum. This effect became greatly manifest when α was close to $+1$ (5.8 dB/cm at $f = 0.5$ beat^{-1} for $\alpha = 0.9$, 11.6 dB/cm for $\alpha = 0.95$, not shown in Fig. 4 *B*). Conversely, negative values of α skewed the spectra toward the left and diminished the effect of CV restitution. However, the gain (in absolute value) remained maximal at $f = 0.5$ beat^{-1}, irrespective of α.

Thus, information about both γ and α can be obtained from the inspection of the transfer function of IBI variations in the frequency domain.

Restitution in the Luo-Rudy model

The analysis of the previous section was conducted using a linear coupled maps model. However, the conduction of the cardiac AP relies on the complex nonlinear dynamics of ion currents. To investigate to what extent the observations regarding APD and CV restitution on the transfer functions in the linear model also apply in the context of a propagated AP based on ion currents, we conducted simulations of conduction in a strand of cells using the modified Luo-Rudy phase 1 model (19).

We first evaluated APD and CV restitution using a conventional S1-S2 pacing protocol. The restitution behavior of the Luo-Rudy model with normal $[K^+]_o$ is shown in Fig. 5, *A* and *B*. The S1-S2 protocol is illustrated in Fig. 5 *A* by superimposed traces of the steady-state AP at a BCL of 120 ms and the APs elicited after the modified S1-S2 interval. Restitution data for APD and CV are presented in Fig. 5 *B* in the form of restitution portraits (6). The dark-shaded curves correspond to steady-state values of APD and CV after all transients had dissipated and the AP during pacing at a constant BCL had fully stabilized. This type of restitution curve has been previously called the dynamic restitution curve (6). The data from the S1-S2 protocols are shown as dotted curves in Fig. 5 *B* (S1-S2 restitution curves), together with their tangents at the corresponding steady-state points. The S1-S2 restitution slopes α and γ were computed from these tangents.

The dynamic APD and CV restitution curves were nonlinear, and the slopes α and γ increased with decreasing BCL/DI. Interestingly, the S1-S2 APD restitution curves were somewhat less steep than the dynamic restitution

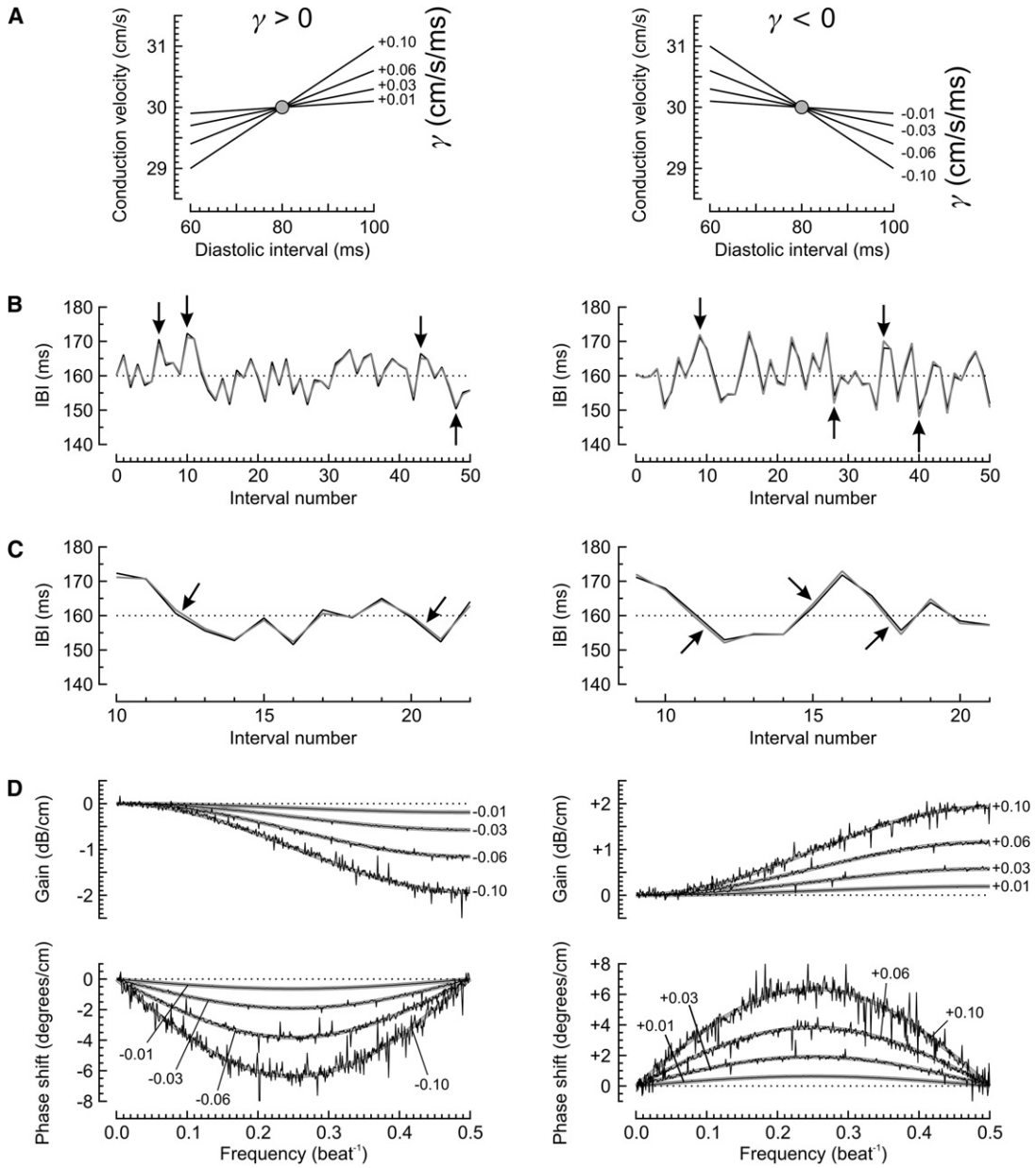

FIGURE 3 Transfer of interbeat interval (IBI) variations in a coupled maps model, in the absence of APD restitution. (*A*) CV restitution functions used in the coupled maps model, with different positive ($\gamma > 0$, *left*) and negative slopes ($\gamma < 0$, *right*), as labeled. The shaded dots represent the steady-state point. (*B*) IBI series at positions $x_1 = 0.25$ cm (*solid*) and $x_2 = 0.75$ cm (*shading*) during stochastic pacing at $x = 0$. IBI variations were attenuated with distance for $\gamma > 0$ (*left*), whereas for $\gamma < 0$, IBI variations were amplified (*right*). The arrows denote variations in which this attenuation/amplification is most visible. (*C*) Subsets of the same IBI series as in *B* on an expanded scale. Relative to the series at x_1, the IBI series at x_2 exhibited a phase lag for $\gamma > 0$ and a phase advance for $\gamma < 0$. The arrows indicate where these phase shifts are most visible. (*D*) Bode plots of normalized gain and phase shift during stochastic pacing (*thin solid traces*, labels denote γ). The normalized frequency responses predicted theoretically are plotted in the rear as thick shaded curves.

curve. This indicates that first-order restitution cannot fully account for the APD restitution behavior of the Luo-Rudy model; if that was the case, the restitution curves should all be superimposed. In contrast, the S1-S2 CV restitution curves were superimposed with the dynamic CV restitution curve despite its pronounced nonlinear aspect, suggesting that CV restitution is reasonably well described by first-order dynamics.

In the past, supernormal excitability (defined as a lesser amount of current or charge necessary to bring cardiac tissue to threshold) was observed for premature stimuli during experiments in reduced $[K^+]_o$ (9,27). To examine whether a reduction of $[K^+]_o$ leads to supernormal conduction of premature stimuli in the Luo-Rudy model, we conducted S1-S2 protocols and constructed the restitution portraits for $[K^+]_o = 2.0$ mmol/L using the same approach as for normal

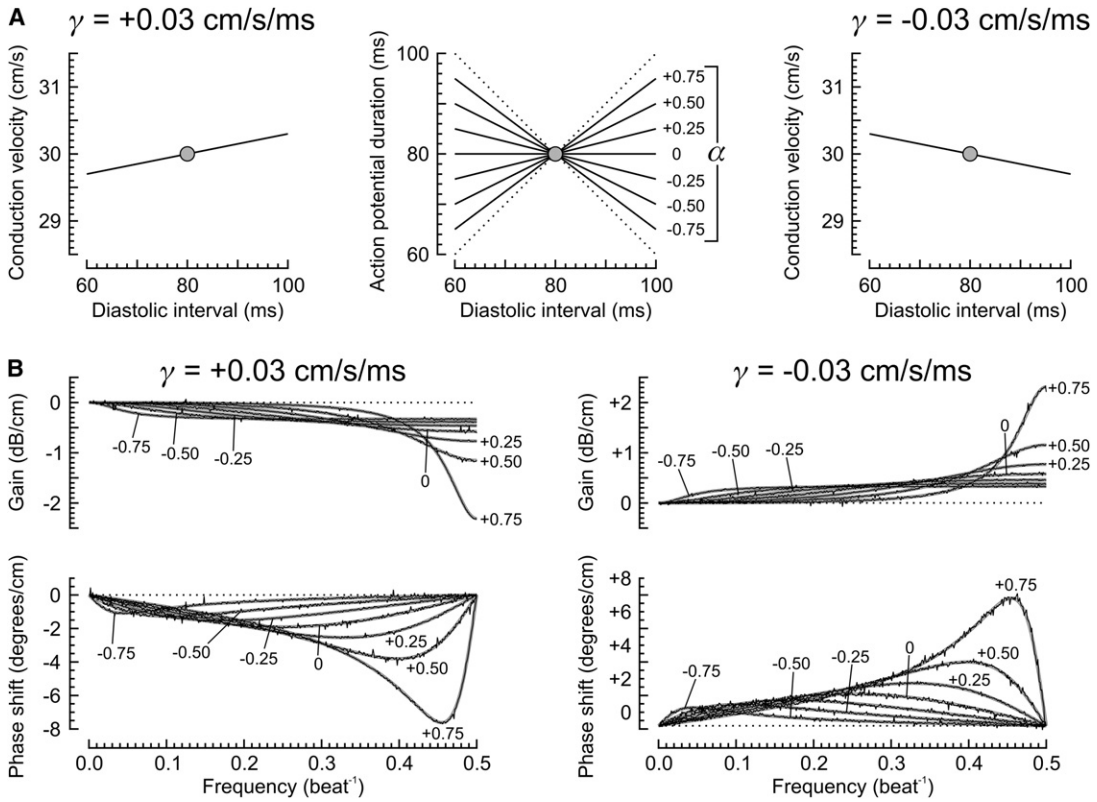

FIGURE 4 Effects of APD restitution on the transfer function of interbeat interval (IBI) variations in a coupled maps model. (*A*) CV restitution functions used in the coupled maps model, with a given positive and negative slope γ (+0.03 cm/s/ms, *left*, and −0.03 cm/s/ms, *right*). While γ was kept constant, the first-order APD restitution slope α (restitution functions in the *middle panel*) was varied in the interval [−1, 1]. The shaded dots represent the steady-state point. (*B*) Bode plots of normalized gain and phase shift during stochastic pacing (*thin solid traces*, labels denote α). The normalized frequency responses predicted theoretically are plotted in the rear as thick shaded curves.

$[K^+]_o$. An example of the S1-S2 protocol is illustrated in Fig. 5 *C* and the restitution portraits are presented in Fig. 5 *D*. The reduction of $[K^+]_o$ decreased the resting membrane potential from −84.6 to −99.8 mV and diminished the magnitude of K^+ currents, leading to a substantial increase of APD. Therefore, the restitution portraits were established using larger BCLs. While the APD restitution portrait was otherwise qualitatively similar to that for normal $[K^+]_o$, the CV restitution portrait was fundamentally different. Both the dynamic and the S1-S2 restitution curves exhibited negative slopes, reflecting supernormal conduction. Moreover, as illustrated in Fig. 5 *D* for BCL = 270 ms, the S1-S2 CV restitution curves exhibited a strong nonlinear behavior at short DIs, with CV decreasing abruptly for DIs <30 ms. Thus, S1-S2 CV restitution curves were biphasic, characterized by a negative slope at long DIs and a positive slope at very short DIs. However, at the corresponding steady-state points, the S1-S2 restitution slope γ was negative for all of the four BCLs tested.

The supernormal phase of the CV restitution curves was explained by the fact that the membrane was still slightly depolarized by a few mV at the onset of premature APs (see Fig. 5 *C*), while the sodium current (I_{Na}) had already recovered from inactivation. As a consequence, the charge necessary to depolarize the membrane to threshold was reduced, leading to accelerated conduction. However, at short S1-S2 intervals, the recovery of I_{Na} was incomplete and the diminished I_{Na} availability prevailed over the smaller charge requirement to reach threshold, leading to a CV restitution curve with a positive slope, as for normal $[K^+]_o$.

Transfer functions of the Luo-Rudy model

The transfer functions of the Luo-Rudy model strand were then determined using the stochastic pacing protocol. Transfer functions of IBI variations were first investigated for normal $[K^+]_o$. The strand was paced until steady state was established at the four different BCLs used in Fig. 5, *A* and *B*, upon which BCL was perturbed with normally distributed beat-to-beat variations with zero mean and an SD of 5 ms. The resulting beat-to-beat variations of the IBI, DI and APD are illustrated in Fig. 6 *A*. The simulations were run for 257 successive APs to obtain series of 256 IBIs at positions x_1 and x_2, from which the frequency responses were computed. The corresponding Bode plots are presented in Fig. 6 *B*, together with the first-order normalized gain and

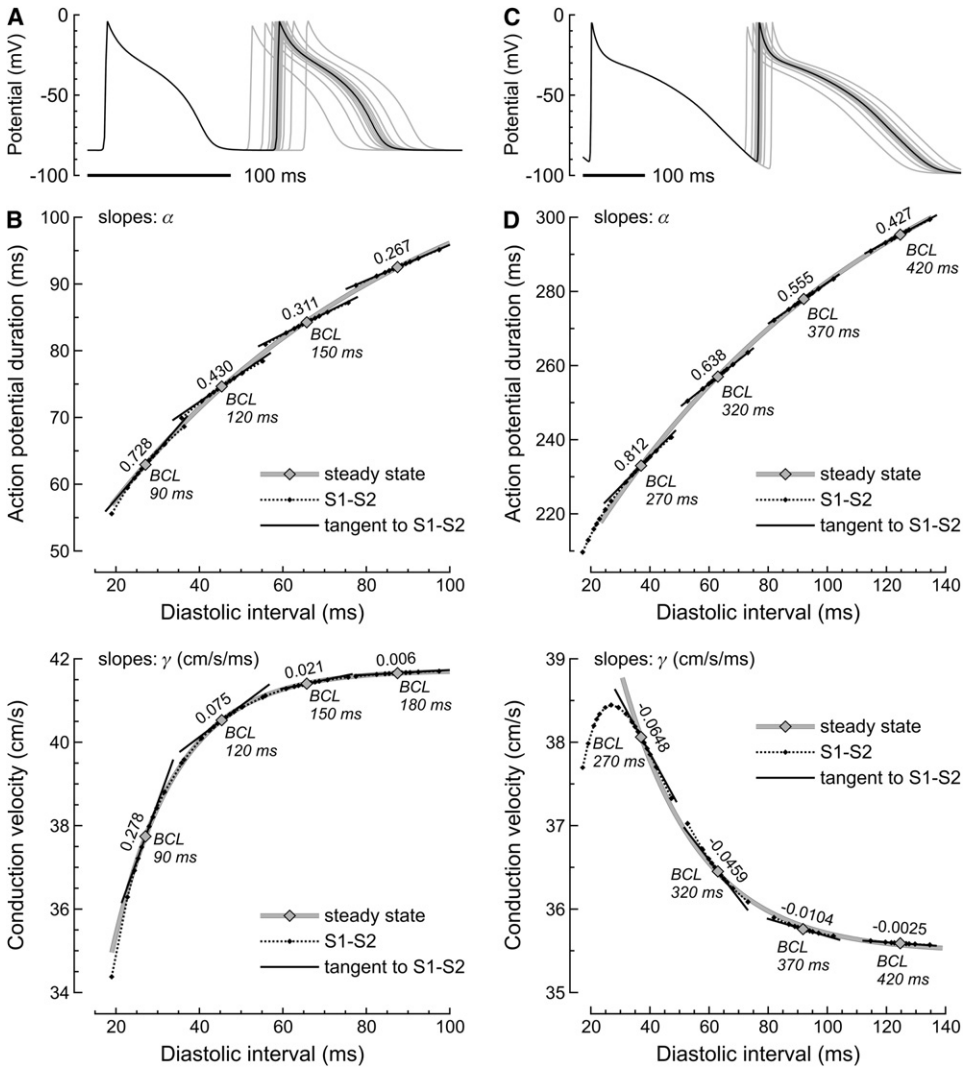

FIGURE 5 Restitution in the Luo-Rudy model investigated with the S1-S2 protocol. (*A*) APs in the center of the strand (normal $[K^+]_o$). (*Solid trace*) APs during steady-state pacing at BCL = 120 ms. (*Shaded traces*) APs after different S1-S2 intervals. (*B*) APD and CV restitution portraits for normal $[K^+]_o$. The large shaded symbols correspond to steady-state values (*fixed points*) at the tested BCLs (*labels* under the *curves*). The dark-shaded curves are exponential fits to these data (dynamic restitution curves). The solid symbols and the corresponding dotted curves represent the S1-S2 restitution relationships for the different BCLs. The slopes (*labels* above the *curves*) of the corresponding tangents correspond to the S1-S2 restitution slopes α and γ. (*C*) Same as *A*, for $[K^+]_o$ = 2.0 mmol/L and for a steady-state BCL of 270 ms. (*D*) APD and CV restitution portraits for low $[K^+]_o$ = 2.0 mmol/L. Same layout as in panel *B*.

phase shift (Eq. 26) based on the control values of α and γ obtained using the S1-S2 protocol (Fig. 5).

The predicted transfer functions were in close agreement with those observed for all of the four BCLs tested. With decreasing mean IBI, the increasing magnitude of the gain and phase shift as well as the progressive skewing of the transfer spectra toward the right witnessed the increasing restitution slopes α and γ. Moreover, this close agreement suggests that the transfer functions were not manifestly altered by the nonlinear aspect of the restitution curves and the higher-order features of APD.

This observation prompted us to investigate whether CV could be predicted and the slopes α and γ determined using the autoregressive-moving-average (ARMA) model $\delta c_{n+1} = \gamma\delta t_n - \alpha\delta c_n$ (Eq. 8). For this purpose, simulations of 30 consecutive APs were conducted using the stochastic pacing protocol. For the analysis, activation times in the center of the strand were interpolated from the activation times at positions x_1 and x_2 as $t = (t(x_1) + t(x_2))/2$ and CV was calculated as $(x_2 - x_1)/(t(x_2) - t(x_1))$. By using this approach, we assumed that an investigator would have no possibility to obtain information about the AP between x_1 and x_2. Indeed, the positions x_1 and x_2 can be imagined as the location of two extracellular recording electrodes placed in close vicinity of a cardiac preparation (or in the heart in vivo), providing an accurate measurement of the time of passage of the successive wavefronts but no information about AP morphology and APD.

Fig. 6 *C* illustrates IBIs, DIs, APDs, and CVs during stochastic pacing at a mean cycle length of 120 ms and an SD of 5 ms. The parameters α and γ of the ARMA model were fit such as to minimize the mean-square residual error on CV prediction. The predicted CV and the residual error are represented in Fig. 6 *C* together with the observed CV. In this example, the best fit was obtained with $\alpha = 0.397$ and $\gamma = 0.073$ cm/s/ms, which lie within 10% of the control values from the S1-S2 protocol (Fig. 5). The square of the correlation coefficient (r^2) between predicted and observed CV was 0.970, indicating that the ARMA model accounted for 97% of the observed variance of CV.

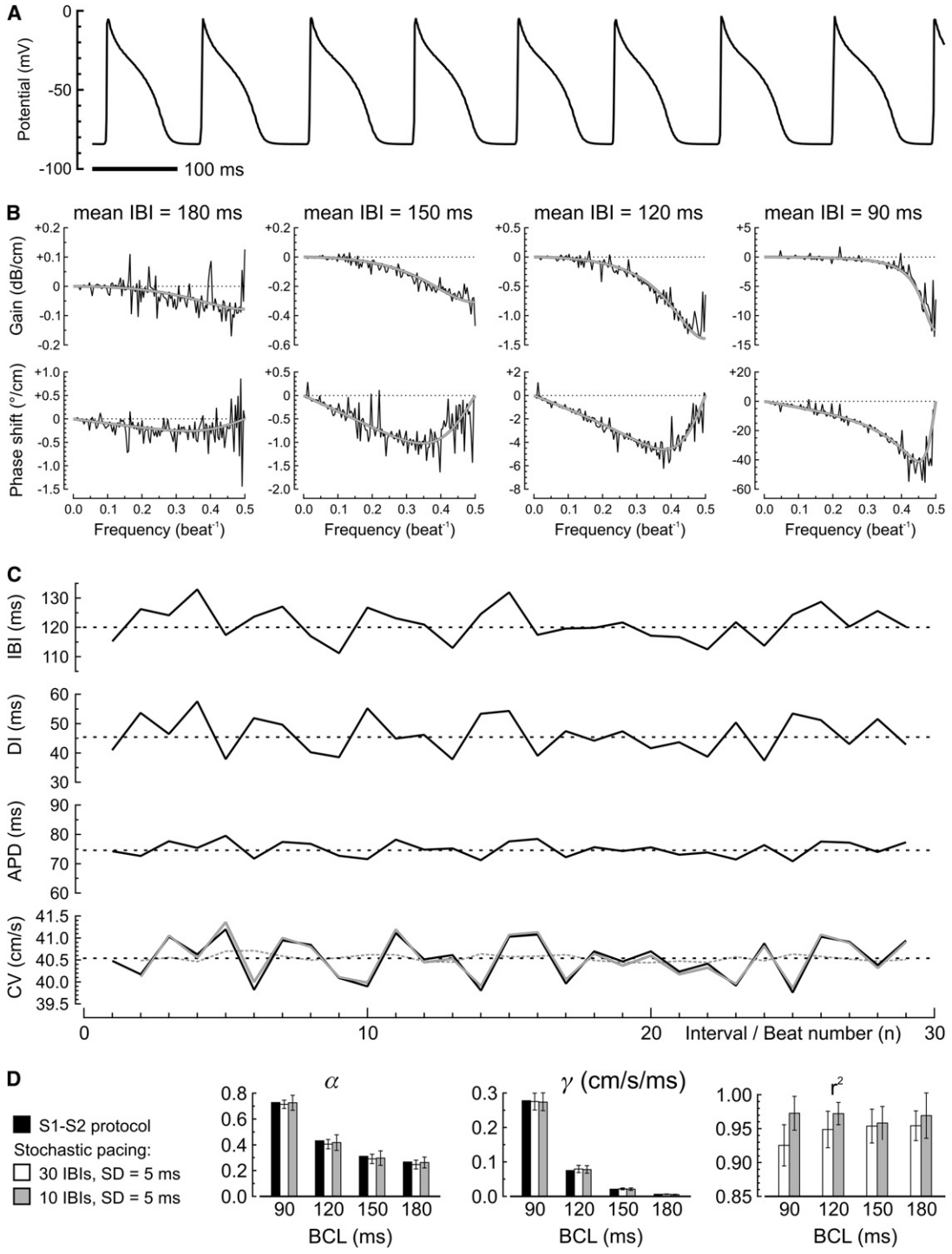

FIGURE 6 Transfer functions and restitution in the Luo-Rudy model during stochastic pacing, with normal $[K^+]_o$. (*A*) Example APs in the center of the strand during pacing at random intervals with a mean of 120 ms and an SD of 5 ms. (*B*) Bode plots of normalized gain and phase shift during stochastic pacing at four different mean IBIs (*thin traces*; note the different ordinates). The shaded curves represent the first-order transfer spectra, predicted theoretically, based on the S1-S2 slopes α and γ determined as described in Fig. 5. (*C*) Series of 30 corresponding IBIs, DIs, APDs, and CVs. Solid traces represent data from the simulation. The CV trace shown in shading represents CV predicted using the best fit first-order ARMA model, and the residual error is shown as a shaded dotted trace. Dotted horizontal lines represent mean values, or the offset to zero for the residual error. (*D*) Determination of α and γ using stochastic pacing versus the S1-S2 protocol (*solid*) and fraction of CV variance predicted by the ARMA model. This determination was conducted using 30 IBIs (*open*) and 10 IBIs (*shaded*), with a SD of pacing intervals of 5 ms. $n = 10$ simulations for each analysis.

The stochastic pacing protocol was then repeated 10 times for each of the tested BCLs. As illustrated in Fig. 6 *D*, the control values of α and γ lay within the mean ± SD of the estimates (*open bars*), and the estimates exhibited a ratio SD/mean in the range of 10%. Also, in all simulations considered together, the first-order ARMA explained >90% of the variance of CV. This analysis thus correctly revealed the increase of both slopes with decreasing BCL. However, the slope α was slightly underestimated because of the nonlinear aspect of restitution and/or higher order restitution characteristics.

To investigate whether the slopes α and γ could be estimated from a smaller number of IBIs, the ARMA model coefficients were identified using a series of 10 IBIs instead of 30 (*shaded bars* in Fig. 6 *D*). On average, reducing the number of IBIs from 30 to 10 yielded the same estimates, but the SD of these estimates increased by ~50%. This indicates that the reliability of the estimates is determined by the number of successive IBIs used for this analysis (see also Data S1).

Fig. 7 illustrates the transfer functions of IBIs and the slopes α and γ obtained via ARMA model identification when $[K^+]_o$ was reduced to 2.0 mmol/L. The Bode plots of the transfer functions (computed from 256 IBIs during stochastic pacing with an SD of 5 ms) are represented in Fig. 7 *A* for the four BCLs used in Fig. 5, *C* and *D*, together with the first-order normalized gain and phase shift based on the control values of α and γ obtained using the S1-S2 protocol. For longer BCLs (420 and 370 ms), the predicted transfer functions were in agreement with the observed ones. However, for shorter BCLs (320 and 270 ms), the observed transfer spectra deviated slightly from the theoretical prediction (*shaded curves*) and were better fit (*dashed curves*) based on the values of α and γ obtained through ARMA model identification using 30 IBIs.

The estimation of α and γ using the ARMA model is further detailed in Fig. 7 *B* in a manner similar to that in Fig. 6 *D*. As for normal $[K^+]_o$, the values obtained using 30 IBIs (*open bars*) provided appropriate estimates of the control S1-S2 restitution slopes for BCL=370 and 420 ms. However, α was manifestly underestimated for BCL = 270 and 320 ms (the control value of α lay >1 SD away from the average of the estimates). ARMA model identification performed, on average, similarly, with 10 IBIs compared to 30 IBIs, and with an SD of the estimates that was again increased by ~50% (*dark shaded bars*). The underestimation for BCL = 320 and 470 ms was therefore not related to the number of IBIs used for analysis. To test whether this underestimation could be related to the pronounced nonlinear aspect of the restitution curves at short BCLs, the same analysis was conducted on 30 IBIs but with an SD of pacing intervals reduced to 1 ms (*light shaded bars*). With this

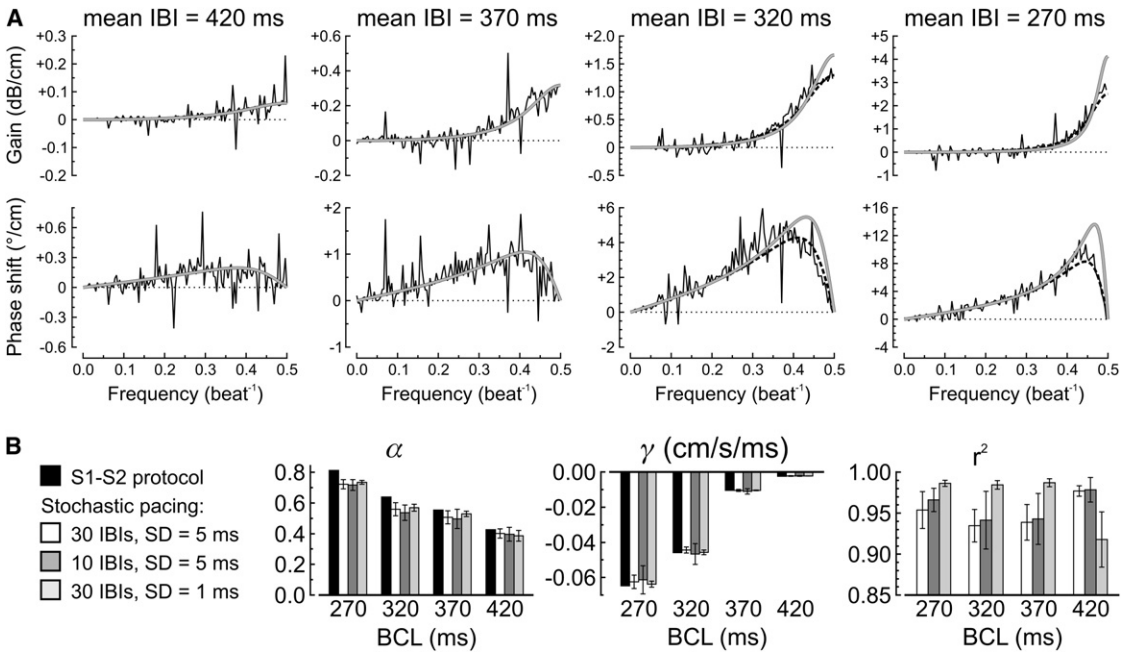

FIGURE 7 Transfer functions and restitution in the Luo-Rudy model during stochastic pacing, with decreased $[K^+]_o$ (2.0 mmol/L). (*A*) Bode plots of normalized gain and phase shift during stochastic pacing at four different mean IBIs with an SD of 5 ms (*thin traces*; note the different ordinates). Same layout as in Fig. 6 *B*. The shaded curves represent the first-order transfer spectra predicted based on the S1-S2 slopes α and γ (Fig. 5). The dotted curves (for IBI = 320 and 270 ms) represent first-order spectra based on α and γ predicted by the ARMA model, as shown in *B*. (*B*) Determination of α and γ using stochastic pacing versus the S1-S2 protocol (*solid*) and fraction of CV variance predicted by the ARMA model. This determination was conducted with an SD of pacing intervals of 5 ms and using 30 IBIs (*open*) and 10 IBIs (*dark shaded*), as well as with an SD of pacing intervals of 1 ms and 30 IBIs (*light shaded*). $n = 10$ simulations for each analysis.

approach, the DIs spanned a narrower portion of the restitution curves around the steady-state point, thus diminishing the influence of nonlinearities. The underestimation of α was partially corrected in this analysis, supporting the notion that strongly nonlinear restitution curves can alter the estimation of their slopes using a linear ARMA model. However, the correction of this underestimation was relatively modest, suggesting that higher-order restitution characteristics may be involved as well (e.g., dependence of APD and/or CV on several previous DIs and APDs).

Normal and supernormal CV restitution in cultured strands of cardiac myocytes

To assess the validity of the theoretical and numerical results in a biological setting, we conducted experiments in strands of cultured rat ventricular myocytes. Using the S1-S2 protocol, we first established CV restitution curves and determined CV restitution slopes at different BCLs. These experiments were carried out under control conditions and in decreased $[K^+]_o$. As illustrated in Fig. 8 *A*, reduction of $[K^+]_o$ from 5.8 to 1.5 mmol/L resulted in slower conduction at each BCL investigated. This reduction of CV is in agreement with the results of previous experimental and modeling studies and can be explained by the more polarized resting membrane potential in decreased $[K^+]_o$ (28,29).

Interestingly, as illustrated by the example CV restitution curves in Fig. 8 *B*, the behavior of CV restitution was radically different in normal versus decreased $[K^+]_o$. In normal $[K^+]_o$, premature impulses propagated slower and postmature impulses propagated faster compared to steady-state impulses at BCL. In contrast, in decreased $[K^+]_o$, premature impulses propagated faster and postmature impulses propagated slower (supernormal conduction of premature impulses). Although the relative differences in CV were small during the S1-S2 protocols, the CV restitution slope γ was >0 in control $[K^+]_o$ (entire 95% confidence interval > 0) in this example and <0 in $[K^+]_o = 1.5$ mmol/L (entire 95% confidence interval < 0), respectively.

We induced supernormal conduction of premature impulses by lowering extracellular potassium concentration to 2.0 mmol/L in $n = 2$ preparations and to $[K^+]_o = 1.5$ mmol/L in $n = 3$ preparations. As illustrated in Fig. 8 *C*, for all experiments in normal $[K^+]_o$, γ was either significantly positive ($p < 0.05$ based on 95% confidence intervals on γ) or not significantly different from 0, but never negative

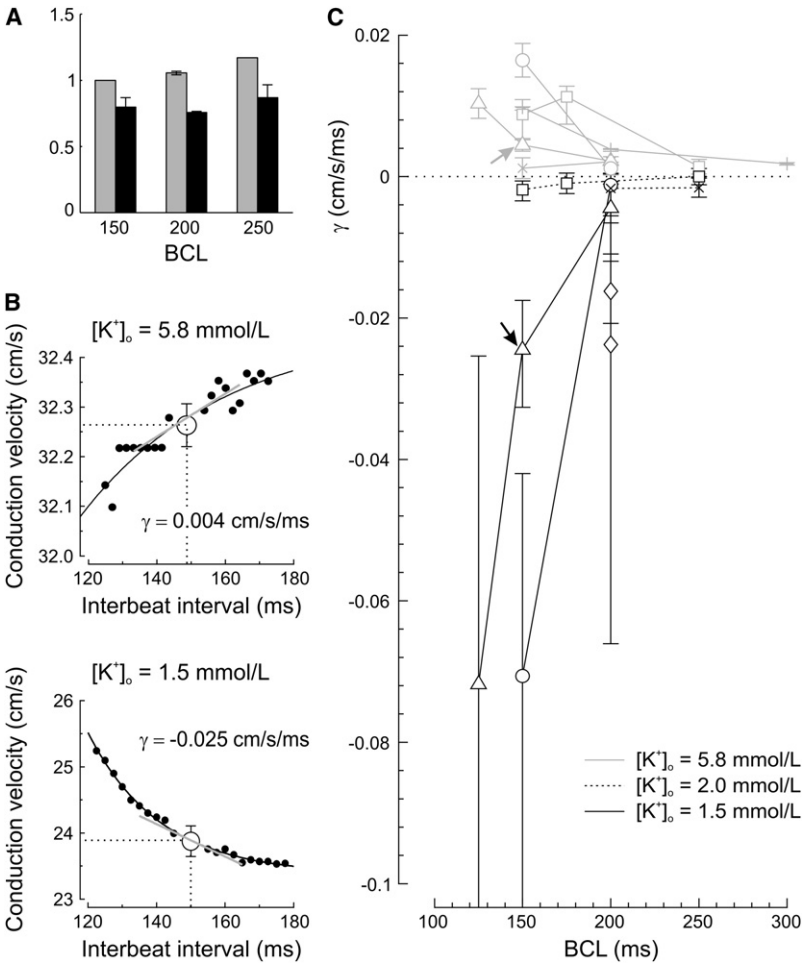

FIGURE 8 CV and CV restitution in strands of cultured cardiac myocytes investigated with the S1-S2 protocol. (*A*) Steady-state CV under control conditions (*shaded*) and in decreased $[K^+]_o$ (1.5 mmol/L, *solid*), for different BCLs. CV was normalized to CV under control conditions at BCL = 150 ms (31.1 ± 2.4 cm/s). (*B*) Example of CV restitution curves under control conditions (*top*) and in decreased $[K^+]_o$ (*bottom*). In both panels, the solid dots represent the CV of the S2 responses and the circle corresponds to the mean CV at steady-state BCL, computed over the last 10 pulses before the beginning of the protocol. The solid curve represents the exponential fit to the data points and the shaded line illustrates the slope γ of the fitted function at IBI = BCL. (*C*) CV restitution slopes γ for $n = 6$ preparations. Identical symbols correspond to the same preparation. The arrows indicate the example shown in panel *B*. Error bars represent 95% confidence intervals.

($n = 13$ experiments in five different preparations). Conversely, in decreased $[K^+]_o$, γ was either significantly negative or not significantly different from 0, but never positive ($n = 11$ experiments in five different preparations). Furthermore, with decreasing BCL, γ exhibited an increasing trend under control conditions and a monotonous decrease (γ became more negative) in low $[K^+]_o$.

Transfer functions of cultured cardiomyocyte strands during stochastic pacing

In six cultured strands, the stochastic stimulation protocol was then used to determine the transfer functions of conduction. For each investigated BCL, the stochastic protocol was executed immediately after the S1-S2 protocol to permit comparison between both protocols. The standard deviation σ of stimulation intervals (10–50 ms) was adjusted to be large relative to the error in the determination of activation times (0.1 ms in our experimental system (30)), but to still result in 1:1 capture of all stimuli. Considerations regarding the influence of measurement noise on the results of our analyses are presented in Data S1. The transfer functions were computed from the activation time series at the electrode closest to the pacing site and the electrode furthest from the stimulation site for which all activation times could be identified. These two electrodes corresponded, respectively, to the most proximal and distal electrodes used for the determination of CV. The transfer functions were then normalized for the length L of the strand between these electrodes ($L =$ 0.25–0.96 cm).

Fig. 9 *A* illustrates interbeat interval series at the proximal and distal electrode for a selected preparation, under control conditions and in low $[K^+]_o$. In this time-domain representation, it is hardly possible to see any differences between the two series under control conditions, and, for the low-$[K^+]_o$ experiment, small differences can only be seen for certain data points (*arrows*). However, as shown in Fig. 9 *B*, the influence of restitution on IBIs is clearly revealed when the relationships between the corresponding series are represented as transfer functions in the frequency-domain. The transfer spectra clearly show that components toward higher frequencies were attenuated under control conditions and amplified in low $[K^+]_o$. Furthermore, phases were delayed in normal $[K^+]_o$ and advanced in low $[K^+]_o$.

The computed transfer functions were fitted with the first-order model (expressions in Eq. 26) by minimizing the mean-square error using a simplex search algorithm (31). This provided estimates for the S1-S2 APD and CV restitution slopes α and γ. For the example illustrated in Fig. 9, *A* and *B*, the estimated slopes were $\alpha = -0.0180$, $\gamma = 0.0083$ cm/s/ms in control $[K^+]_o$ and $\alpha = 0.2021$, $\gamma = -0.0231$cm/s/ms in low $[K^+]_o$, respectively.

In Fig. 9 *C*, the estimated slopes α and γ are reported for all stochastic pacing experiments. In agreement with the results obtained with the S1-S2 protocol, the computed values of γ were all strictly positive under control conditions ($n =$ 15 experiments in $n = 6$ preparations) and strictly negative in low $[K^+]_o$ ($n = 8$ experiments in $n = 3$ preparations). It should be noted that the estimates of α are reliable only for BCL $\leq$ 200, since for BCL $>$ 200, γ is close to zero and the function $\Phi_L(f)$ in Eq. 26 is therefore small (in absolute value). For this reason, the extremum of $\Phi_L(f)$, determined by α, is difficult to identify.

Comparison of the CV restitution slopes obtained with the two protocols

Both pacing protocols were applied together in $n = 4$ cultures to obtain the slope of CV restitution at one or more different BCLs and $[K^+]_o$. This provided a total of 17 data points. In Fig. 9 *C*, the values of γ obtained with the stochastic protocol are plotted against the corresponding values obtained with the control S1-S2 protocol. If both protocols provided an identical estimate of the slope γ, all points would lie on the identity line $\gamma_{S1-S2} = \gamma_{\text{stochastic}}$. Two points lay outside the 95% confidence bounds and were considered as outliers. The linear regression on the remaining points provided a relationship given by $\gamma_{S1-S2} = 1.0278\gamma_{\text{stochastic}} - 0.00038$, with $r = 0.9674$. This indicates that there is an accurate correspondence between the slopes γ obtained with the S1-S2 protocol and those obtained by fitting the transfer function with a first-order model, which suggests that first-order restitution represents a good model for local stability. Moreover, this indicates that both methods give accurate results: only an identical systematic error in both methods could lead to this close correspondence. Since the two methods are fundamentally different, this appears, however, unlikely.

DISCUSSION

The velocity with which the action potential propagates in cardiac tissue is rate-dependent, and therefore it can change from beat to beat. From this, it immediately follows that the time interval between two successive wavefronts propagating at different velocities is not spatially constant. Therefore, the interbeat interval depends on the location where it is observed. As a result, different interbeat intervals at different positions will lead to different ionic behaviors at the cellular level, which in turn, will affect CV. The sequence of interbeat intervals and how this sequence is modulated as a function of position thus reflects this dynamic feedback between restitution at the cellular level (APD, Ca^{2+}) and at the tissue level (CV).

Modulation of interbeat intervals and implications for arrhythmogenesis

Based on well-established notions of linear systems theory, which provides specifically adapted tools to assess stability (32), we explored how interbeat interval variations are

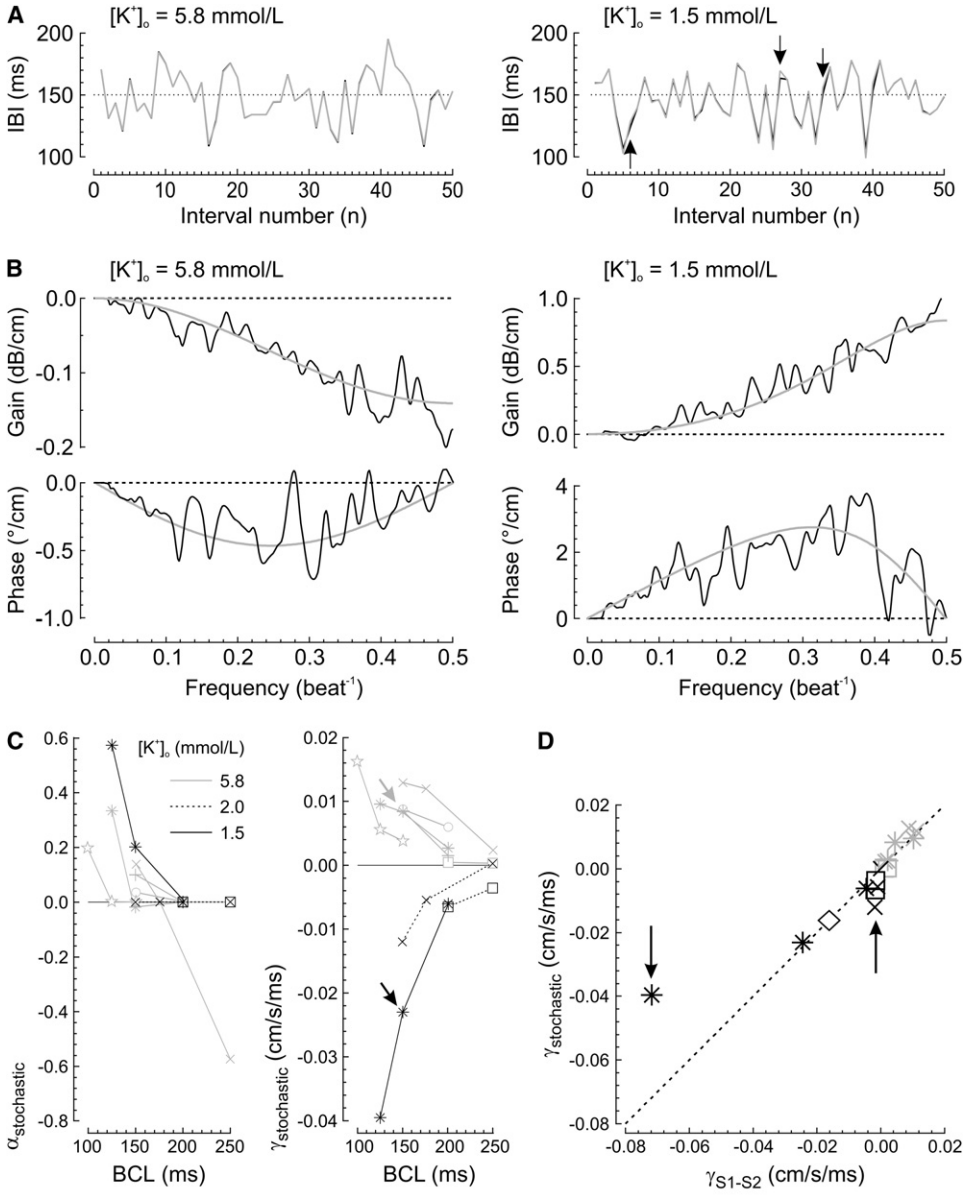

FIGURE 9 Transfer functions in strands of cultured cardiac myocytes. (*A*) Interbeat interval time series during stochastic pacing of a preparation under control conditions (*left*, mean BCL, 150 ms; SD of BCL, 25 ms) and in low $[K^+]_o$ (*right*, mean BCL, 150 ms; SD of BCL, 20 ms). The solid traces represent the time series at the proximal electrode and the overlaid shaded traces are the time series at the distal electrode (interelectrode distance, 0.96 cm). In this time-domain representation, small differences between the two series are not visible in control $[K^+]_o$ and only barely visible in low $[K^+]_o$ (*arrows*). (*B*) Transfer functions corresponding to the experimental data shown in *A* (*solid traces*). The shaded curves represent fits to these data using the theoretical transfer function stated in Eqs. 26. (*C*) Values of α and γ estimated from the fits of Eqs. 26 to the transfer functions in various $[K^+]_o$. Identical markers correspond to the same preparation. The shaded and solid arrows mark the example shown in *A* and *B* for control and low $[K^+]_o$ respectively. (*D*) Comparison of the values of γ computed from the transfer functions and from the S1-S2 protocol. The dotted line is the identity line. Outliers are indicated by arrows.

modulated in the spatial dimension by the restitution properties of cardiac tissue. Pacing at stochastic interbeat intervals represents the key element of our approach. As predicted by our theory, we observed in both the Luo-Rudy simulations and the cardiomyocyte strands that a positive restitution slope γ attenuates variations of interbeat intervals in a frequency-dependent manner, while a negative γ amplifies them. The maximal effect occurs at the frequency of alternans, per definition once every two beats.

This finding has two important implications for arrhythmogenesis. First, attenuation of alternans in the presence of $\gamma > 0$ (which is the case in normal circumstances) suggests that this property of cardiac tissue represents a protective mechanism: if alternans is generated at a given place in the heart on the pathway of AP propagation, this attenuation property will filter alternans out at distal sites, thus stabilizing the activation pattern. Second, amplification of alternans in the presence of $\gamma < 0$ indicates that supernormal conduction of premature impulses represents in itself a mechanism potentiating alternans and arrhythmogenesis. The simulations using the coupled maps model showed that this amplification occurs even in the complete absence of APD restitution. This complements our understanding of alternans with the notion that alternans does not necessarily originate solely from restitution properties of APD at the cellular level.

In both the Luo-Rudy simulations and the experiments, supernormal conduction led to a gain in the range of $+1$ dB/cm at $f = 0.5$ beat^{-1}. This value, transposed to the scale of the human heart (~10 cm), suggests that supernormal conduction with similar characteristics may amplify small IBI

variations (that could occur spontaneously) by a factor 10. This is likely to exert a significant impact on the stability of cardiac excitation and the generation of arrhythmias.

Our mathematical analysis revealed that the transfer spectra of interbeat intervals are markedly affected by APD restitution. In a first-order formalism, a positive S1-S2 restitution slope α (which is usually the case in most cardiac tissues) shifts the transfer spectrum toward the right and dramatically increases the filtering effect of cardiac tissue at $f = 0.5$ beat^{-1}. This prediction was verified in both the Luo-Rudy simulations and the cultured cardiomyocyte strands. Once more, this finding bears an implication for arrhythmogenesis. While steep APD restitution slopes are usually considered deleterious because of their correlation with alternans, our finding indicates that a positive slope α also enhances the protective role of a positive γ, as described above. Thus, a steep APD restitution curve may be both deleterious and beneficial at the same time. The net effect in terms of arrhythmia initiation will then depend, among other factors, on the spatial distribution and heterogeneity of restitution properties. This two-faced effect may have consequences for the development and use of antiarrhythmic drugs that affect APD restitution.

New strategies to investigate electrical restitution

It is logically assumed that the investigation of APD restitution requires measurements of APD. In experimental settings, APD is typically measured using membrane potential recordings with conventional micropipettes or using voltage-sensitive dyes. While these two approaches are routinely employed in experimental electrophysiology, these two techniques cannot be applied in vivo, and a fortiori in a clinical setting. Cardiac activation can also be investigated using extracellular electrodes (e.g., mapping catheters in clinical practice), but determination of APD from extracellular electrograms is often difficult or impossible. Our analyses show that, by using stochastic pacing, an estimate of the S1-S2 restitution slope α can be obtained without measuring APD. Thus, more information can be efficiently obtained about the electrical function of cardiac tissue by using stochastic pacing, compared to a simpler protocol such as the S1-S2.

The strength of our analysis resides in its simplicity and in the possibility to extend it to any cardiac preparation, or model, or even in vivo, in a flexible manner. In its fundamental form, it only requires two distinct sites at which the time of passage of the action potential is captured. Stochastic pacing protocols are easy to implement and the computation of the spectrum of the transfer function is straightforward. Undeniably, the great challenge will reside in the interpretation of the transfer function and how it is influenced, e.g., by heterogeneous tissue and conduction in two- and three-dimensional media (see below). Beyond these challenges, the analysis of the transfer function may then offer perspectives for both research and clinical practice.

Possible developments of the mathematical framework

Cardiac tissue is intrinsically heterogeneous in both the healthy and diseased heart. This heterogeneity is apparent in the level of expression of different ion channels across the myocardial wall (33) and between different cardiac chambers (34). Cardiac tissue is also histologically heterogeneous (35–37). The presence of myofibroblasts in cardiac tissue introduces a further level of tissue heterogeneity (38). Therefore, in cardiac tissue, APD and CV restitution characteristics are not absolutely uniform but exhibit heterogeneities and gradients. When determined between two points x_1 and x_2, the transfer function of interbeat intervals reflects the aggregate restitution characteristics over the segment x_1x_2. If cardiac excitation is mapped with multiple electrodes, comparison of the transfer functions between pairs of adjacent electrodes may be able to reveal significant discontinuities or gradients and identify critical sites where conduction is most prone to alternans, marginally stable, or where the first-order APD restitution parameter α is the closest to 1.

Besides the influence of the heterogeneous nature of cardiac tissue on AP propagation, conduction is also modulated by wavefront curvature in two- or three-dimensional tissue (39,40). Even in uniform isotropic tissue, a convex wavefront propagates slower compared to a planar wave because of the divergence of electrotonic current at the wavefront (39,40). Assuming that the CV restitution curve of a convex wavefront would correspond to a compressed image of the reference curve of a planar wave, the factor γ/c^{*2} in Eqs. 17–26 would increase because of the power of 2 in the denominator. This would magnify the contribution of CV restitution to the transfer function of IBIs. Moreover, the convergence or electrotonic current at the curved repolarization tail (wave tail) may increase APD, which would lead, under normal conditions, to a leftward shift of the steady-state points into steeper regions of both restitution curves. For convex wavefronts, the transfer spectrum may therefore correspond to a situation with larger α and γ compared to planar propagation. For concave wavefronts, the opposite considerations would apply.

In addition, conduction is also modulated by tissue anisotropy, fiber curvature, and fiber rotation (41,42). In this context, approaches based on the formulation of eikonal-curvature equations (43) combined with differential geometry may therefore be appropriate to generalize our framework.

Comparison with previous studies

In a previous work using the same experimental preparation, we observed that the APD S1-S2 restitution slope α is slightly negative (~ -0.02) at a basic cycle length of 500 ms (26). This cycle length was, however, much longer than that used in this study. In a further work (23), we used first-order restitution theory to estimate the restitution slope α during reentry in rings of cultured cardiac cells based

on damped cycle length oscillations after resetting stimuli. During stable reentry at a period of 129 ± 31 ms, α amounted to 0.29 ± 0.23. In this study, the estimates of α ranged between 0 and 0.35 (in control $[K^+]_o$) for the corresponding mean interbeat intervals (100, 125, and 150 ms in Fig. 9 *C*. The observations in this study regarding α are thus in agreement with our previous results.

Study limitations

Our study suffers from the limitation that we did not record transmembrane potentials in our cultures and thus we did not have a basis to directly compare APD restitution properties established by direct APD measurements (e.g., with micropipette recordings) with the results from our analysis of transfer functions.

Although the theoretical treatment presented here can incorporate any higher-order extension, it is based on a linearization of the restitution functions around their operating points. As illustrated in Fig. 7, the accuracy of the results is directly linked to the accuracy of this linear approximation. Because of the nonlinear nature of restitution, our analysis therefore requires the stochastic variations of IBIs to be sufficiently small. The amplitude of the stochastic variations must therefore be carefully chosen, in particular in experimental settings in which a tradeoff must be achieved among the amplitude of these variations, measurement error, and the expected nonlinearity of restitution. However, when nonlinearities start to exert a noticeable influence but remain weak (i.e., typically as long as the restitution functions remain invertible), techniques making use, e.g., of a Volterra series (44) can be used to extend the result represented here, leaving the framework intact.

As suggested recently, beat-to-beat variations of APD may also result from the stochastic variations of plateau currents due to the open-close behavior of single channels (45). We did not incorporate this type of variability in our simulations. However, with a few modifications, our mathematical framework would permit us to incorporate this variability in further studies and to evaluate its influence on transfer functions.

Finally, our analysis requires that the dynamics governing the investigated system remain stationary during the period of observation. It remains therefore to be shown to what extent our analysis remains applicable in the presence of a high level of nonstationarity.

SUPPLEMENTARY MATERIAL

Methods and one figure are available at http://www.biophysj.org/biophysj/supplemental/S0006-3495(08)00033-7.

We express our gratitude to Prof. Stephan Rohr for the design and support of the experimental setup and to Regula Flückiger Labrada for the preparation of the cultures.

This study was supported by the Swiss National Science Foundation (grants No. 3100A0-100285 and No. 310000-120514 to J.P.K.).

REFERENCES

1. Qu, Z., J. N. Weiss, and A. Garfinkel. 1999. Cardiac electrical restitution properties and stability of reentrant spiral waves: a simulation study. *Am. J. Physiol.* 276:H269–H283.
2. Weiss, J. N., A. Garfinkel, H. S. Karagueuzian, Z. Qu, and P. S. Chen. 1999. Chaos and the transition to ventricular fibrillation: a new approach to antiarrhythmic drug evaluation. *Circulation.* 99:2819–2826.
3. Garfinkel, A., Y. H. Kim, O. Voroshilovsky, Z. Qu, J. R. Ki, et al. 2000. Preventing ventricular fibrillation by flattening cardiac restitution. *Proc. Natl. Acad. Sci. USA.* 97:6061–6066.
4. Nolasco, J. B., and R. W. Dahlen. 1968. A graphic method for the study of alternation in cardiac action potentials. *J. Appl. Physiol.* 25:191–196.
5. Banville, I., N. Chattipakorn, and R. A. Gray. 2004. Restitution dynamics during pacing and arrhythmias in isolated pig hearts. *J. Cardiovasc. Electrophysiol.* 15:455–463.
6. Kalb, S. S., H. M. Dobrovolny, E. G. Tolkacheva, S. F. Idriss, W. Krassowska, et al. 2004. The restitution portrait: a new method for investigating rate-dependent restitution. *J. Cardiovasc. Electrophysiol.* 15:698–709.
7. Gilmour, R. F., Jr., N. F. Otani, and M. A. Watanabe. 1997. Memory and complex dynamics in cardiac Purkinje fibers. *Am. J. Physiol. Heart Circ. Physiol.* 272:H1826–H1832.
8. Fenton, F. H., S. J. Evans, and H. M. Hastings. 1999. Memory in an excitable medium: a mechanism for spiral wave breakup in the low-excitability limit. *Phys. Rev. Lett.* 83:3964–3967.
9. Chialvo, D. R., D. C. Michaels, and J. Jalife. 1990. Supernormal excitability as a mechanism of chaotic dynamics of activation in cardiac Purkinje fibers. *Circ. Res.* 66:525–545.
10. Tolkacheva, E. G., D. G. Schaeffer, D. J. Gauthier, and W. Krassowska. 2003. Condition for alternans and stability of the 1:1 response pattern in a ''memory'' model of paced cardiac dynamics. *Phys. Rev. E Stat. Nonlin. Soft Matter Phys.* 67:031904.
11. Kalb, S. S., E. G. Tolkacheva, D. G. Schaeffer, D. J. Gauthier, and W. Krassowska. 2005. Restitution in mapping models with an arbitrary amount of memory. *Chaos.* 15:23701.
12. Weiss, J. N., A. Karma, Y. Shiferaw, P. S. Chen, A. Garfinkel, et al. 2006. From pulsus to pulseless: the saga of cardiac alternans. *Circ. Res.* 98:1244–1253.
13. Sato, D., Y. Shiferaw, Z. Qu, A. Garfinkel, J. N. Weiss, et al. 2007. Inferring the cellular origin of voltage and calcium alternans from the spatial scales of phase reversal during discordant alternans. *Biophys. J.* 92:L33–L35.
14. Choi, B. R., T. Liu, and G. Salama. 2004. Adaptation of cardiac action potential durations to stimulation history with random diastolic intervals. *J. Cardiovasc. Electrophysiol.* 15:1188–1197.
15. Wu, R., and A. Patwardhan. 2006. Mechanism of repolarization alternans has restitution of action potential duration dependent and independent components. *J. Cardiovasc. Electrophysiol.* 17:87–93.
16. Wu, R., and A. Patwardhan. 2007. Effects of rapid and slow potassium repolarization currents and calcium dynamics on hysteresis in restitution of action potential duration. *J. Electrocardiol.* 40:188–199.
17. Wu, R., and A. Patwardhan. 2004. Restitution of action potential duration during sequential changes in diastolic intervals shows multimodal behavior. *Circ. Res.* 94:634–641.
18. Ljung, L. 1999. System Identification—Theory for the User, 2nd Ed. Prentice Hall, Upper Saddle River, NJ.
19. Luo, C. H., and Y. Rudy. 1991. A model of the ventricular cardiac action potential. Depolarization, repolarization, and their interaction. *Circ. Res.* 68:1501–1526.
20. Spear, J. F., and E. N. Moore. 1974. Supernormal excitability and conduction in the His-Purkinje system of the dog. *Circ. Res.* 35:782–792.
21. Curtain, R., and H. Zwart. 1995. An Introduction to Infinite-Dimensional Linear Systems Theory. Springer-Verlag, New York.
22. Kubrusly, C. 1977. Distributed parameter system identification—a survey. *Int. J. Control.* 26:595–605.

23. Munteanu, A., A. A. Kondratyev, and J. P. Kucera. 2008. Analysis of damped oscillations during reentry: a new approach to evaluate cardiac restitution. *Biophys. J.* 94:1094–1109.

24. Shaw, R. M., and Y. Rudy. 1997. Ionic mechanisms of propagation in cardiac tissue. Roles of the sodium and L-type calcium currents during reduced excitability and decreased gap junction coupling. *Circ. Res.* 81:727–741.

25. Rohr, S., R. Flückiger-Labrada, and J. Kucera. 2003. Photolithographically defined deposition of attachment factors as a versatile method for patterning the growth of different cell types in culture. *Pflugers Arch.* 446:125–132.

26. Kondratyev, A. A., J. G. Ponard, A. Munteanu, S. Rohr, and J. P. Kucera. 2007. Dynamic changes of cardiac conduction during rapid pacing. *Am. J. Physiol. Heart Circ. Physiol.* 292:H1796–H1811.

27. Davidenko, J. M., R. J. Levi, G. Maid, M. V. Elizari, and M. B. Rosenbaum. 1990. Rate dependence and supernormality in excitability of guinea pig papillary muscle. *Am. J. Physiol.* 259:H290–H299.

28. Shaw, R. M., and Y. Rudy. 1997. Electrophysiologic effects of acute myocardial ischemia. A mechanistic investigation of action potential conduction and conduction failure. *Circ. Res.* 80:124–138.

29. Rohr, S., J. P. Kucera, and A. G. Kléber. 1998. Slow conduction in cardiac tissue. I. Effects of a reduction of excitability versus a reduction of electrical coupling on microconduction. *Circ. Res.* 83:781–794.

30. Ponard, J. G., A. A. Kondratyev, and J. P. Kucera. 2007. Mechanisms of intrinsic beating variability in cardiac cell cultures and model pacemaker networks. *Biophys. J.* 92:3734–3752.

31. Nelder, J., and R. Mead. 1965. A simplex method for function minimization. *Comput. J.* 7:308–313.

32. Rugh, W. 1996. Linear System Theory, 2nd Ed. Prentice Hall, Upper Saddle River, NJ.

33. Antzelevitch, C. 2001. Transmural dispersion of repolarization and the T wave. *Cardiovasc. Res.* 50:426–431.

34. Samie, F. H., O. Berenfeld, J. Anumonwo, S. F. Mironov, S. Udassi, et al. 2001. Rectification of the background potassium current: a determinant of rotor dynamics in ventricular fibrillation. *Circ. Res.* 89:1216–1223.

35. LeGrice, I. J., B. H. Smaill, L. Z. Chai, S. G. Edgar, J. B. Gavin, et al. 1995. Laminar structure of the heart: ventricular myocyte arrangement and connective tissue architecture in the dog. *Am. J. Physiol.* 269:H571–H582.

36. Spach, M., and P. Dolber. 1986. Relating extracellular potentials and their derivatives to anisotropic propagation at a microscopic level in human cardiac muscle. Evidence for electrical uncoupling of side-to-side fiber connections with increasing age. *Circ. Res.* 58:356–371.

37. de Bakker, J., F. Van Capelle, M. Janse, S. Tasseron, J. Vermeulen, et al. 1993. Slow conduction in the infarcted human heart: zigzag course of activation. *Circulation.* 88:915–926.

38. Miragoli, M., G. Gaudesius, and S. Rohr. 2006. Electrotonic modulation of cardiac impulse conduction by myofibroblasts. *Circ. Res.* 98:801–810.

39. Cabo, C., A. M. Pertsov, W. T. Baxter, J. M. Davidenko, R. A. Gray, et al. 1994. Wave-front curvature as a cause of slow conduction and block in isolated cardiac muscle. *Circ. Res.* 75:1014–1028.

40. Fast, V., and A. G. Kléber. 1996. Role of wavefront curvature in propagation of cardiac impulse. *Cardiovasc. Res.* 33:258–271.

41. Henriquez, C. S., A. L. Muzikant, and C. K. Smoak. 1996. Anisotropy, fiber curvature, and bath loading effects on activation in thin and thick cardiac tissue preparations: simulations in a three-dimensional bidomain model. *J. Cardiovasc. Electrophysiol.* 7:424–444.

42. Spach, M. S. 1999. Anisotropy of cardiac tissue: a major determinant of conduction? J. Cardiovasc. Electrophysiol. 10:887–890.

43. Keener, J. P. 1991. An eikonal-curvature equation for action potential propagation in myocardium. *J. Math. Biol.* 29:629–651.

44. Rugh, W. 1981. Nonlinear System Theory: The Volterra/Wiener Approach. The Johns Hopkins University Press, Baltimore, MD.

45. Zaniboni, M., F. Cacciani, and N. Salvarani. 2007. Temporal variability of repolarization in rat ventricular myocytes paced with time-varying frequencies. *Exp. Physiol.* 92:859–869.